

Stability of the ultrafine-grained microstructure in silver processed by ECAP and HPT

Zoltán Hegedűs · Jenő Gubicza · Megumi Kawasaki ·
Nguyen Q. Chinh · János L. Lábár ·
Terence G. Langdon

Received: 25 October 2012 / Accepted: 24 December 2012 / Published online: 5 January 2013
© Springer Science+Business Media New York 2013

Abstract The high-temperature thermal stability of the ultrafine-grained (UFG) microstructures in low stacking fault energy silver was studied by differential scanning calorimetry (DSC). The UFG microstructures were achieved by equal-channel angular pressing (ECAP) and high-pressure torsion (HPT) at room temperature (RT). The defect structure in the as-processed samples was examined by electron microscopy and X-ray line profile analysis. The stored energy calculated from the defect densities was compared to the heat released during DSC. The sum of the energies stored in grain boundaries and dislocations in the ECAP-processed samples agreed with the heat released experimentally within the experimental error. The temperature of the DSC peak maximum decreased while the

released heat increased with increasing numbers of ECAP passes. The released heat for the specimen processed by one revolution of HPT was much smaller than after 4–8 passes of ECAP despite the 2 times larger dislocation density measured by X-ray line profile analysis. This dichotomy was caused by the heterogeneous sandwich-like microstructure of the HPT-processed disk: about 175 μm wide surface layers on both sides of the disk exhibited a UFG microstructure while the internal part was recrystallized, thereby yielding a relatively small released heat.

Introduction

Severe plastic deformation (SPD) is an effective way to produce bulk ultrafine-grained (UFG) metals and alloys free of contamination and porosity. The most frequently used methods of SPD are equal-channel angular pressing (ECAP) and high-pressure torsion (HPT) [1–4]. The stability of the UFG microstructures processed by these procedures is a prerequisite in the practical applications of these materials. The high-temperature thermal stability is usually investigated by differential scanning calorimetry (DSC) [5–7]. In these experiments, the recovery of the defect structure and the recrystallization yield an evolution of an exothermic peak on the thermogram at a temperature of about $0.3\text{--}0.4 \times T_m$, where T_m is the absolute melting point [8–11]. An inspection of the shift of the exothermic peak as a function of the heating rate showed that for pure UFG face centered cubic (fcc) metals the activation energy of recovery/recrystallization is between $0.3\text{--}0.6 \times Q_{\text{self}}$, where Q_{self} is the activation energy of self-diffusion, irrespective of the SPD processing method and the properties of the materials (e.g., stacking fault energy, SFE) [7, 8, 12–19]. This result suggests that the recovery and

Z. Hegedűs · J. Gubicza (✉) · N. Q. Chinh
Department of Materials Physics, Eötvös Loránd University,
Pázmány Péter s. 1/A, 1117 Budapest, Hungary
e-mail: gubicza@metal.elte.hu

M. Kawasaki · T. G. Langdon
Departments of Aerospace and Mechanical Engineering
and Materials Science, University of Southern California,
Los Angeles, CA 90089-1453, USA

M. Kawasaki
Division of Materials Science and Engineering, Hanyang
University, 17 Haengdang-dong, Seongdong-gu, Seoul 133-791,
South Korea

J. L. Lábár
Research Institute for Technical Physics and Materials Science,
Research Centre for Natural Sciences, Hungarian Academy
of Sciences, P.O. Box 49, 1525 Budapest, Hungary

T. G. Langdon
Materials Research Group, Faculty of Engineering
and the Environment, University of Southampton,
Southampton SO17 1BJ, UK

recrystallization is controlled by vacancy migration along grain boundaries and dislocations, since the activation energy for both mechanisms is also about one-half of the activation energy for self-diffusion [20, 21].

Most of the research on the thermal stability of UFG metals was performed on fcc metals with medium or high SFE. However, it has already been shown that SFE has a very significant effect on the stability of the UFG microstructures [22–28]. For instance, recovery and recrystallization were observed in ECAP- and HPT-processed Ag, Au, and Cu samples having low or medium SFE during their storage at RT [24–28]. This phenomenon referred to as self-annealing has already been investigated in Ag with an extremely low SFE [27, 28]. At the same time, the high temperature stability of the UFG microstructure in SPD-processed silver has received only limited attention [19].

In this paper, the high-temperature thermal stability of ECAP- and HPT-processed UFG silver was investigated by DSC. The defect structure in the as-processed samples was determined by X-ray line profile analysis (XLPA), transmission electron microscopy (TEM) and scanning electron microscopy (SEM), and then related to the heat released during annealing in DSC.

Experimental materials and procedures

Samples of 4 N purity silver were manufactured by American Elements. The alloying elements and their concentrations are listed in [19]. The billets with ~ 70 mm in length and 10 mm in diameter were annealed at 741 K (corresponding to $0.6 \times T_m$) for 1 h. The annealed samples were processed through 1, 4, 8, and 16 passes of ECAP at RT with a pressing velocity of 8 mm s^{-1} . The pressing was conducted using route B_c where the billet is rotated in the same sense by 90° about its longitudinal axis after each pass [29]. The ECAP die had an internal channel angle of 90° and an outer arc of curvature of 20° . In this configuration one pass corresponds to an equivalent strain of ~ 1 [30]. One turn of HPT was also applied on cylinders ~ 10 mm in diameter and ~ 0.8 mm in thickness. The applied pressure was 6 GPa and the deformation was carried out at RT with a rotation rate of 1 rpm. The two anvils of the HPT device have shallow central depressions on their outer surfaces, with depths of 0.25 mm and diameters of 10 mm at the bottom, and with slightly inclined walls having outer inclinations of 22° , as shown in Fig. 1. The thickness of the sample processed by one revolution of HPT was 0.65 mm after releasing the applied pressure.

The microstructure immediately after SPD was examined by XLPA on transverse sections cut perpendicular to the axes of the ECAP-processed billets and at the center, half-radius and periphery of the surface of the disk

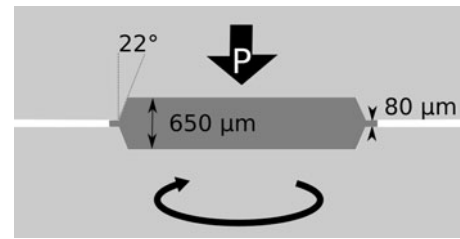


Fig. 1 Schematic illustration of the geometry of the anvils and the workpiece used in HPT-processing. The thickness of the sample processed by one revolution of HPT was about $650 \mu\text{m}$ after releasing the applied pressure

processed by HPT. The measurements of the X-ray diffraction lines were performed using a special high-resolution diffractometer (Nonius FR591) with $\text{CuK}\alpha_1$ radiation ($\lambda = 0.15406 \text{ nm}$). The line profiles were evaluated using the convolutional multiple whole profile (CMWP) fitting procedure [31, 32]. In this method, the diffraction pattern is fitted by the sum of a background spline and the convolution of the instrumental pattern and the theoretical line profiles related to the crystallite size, dislocations, and twin faults. The details of the CMWP procedure are available elsewhere [31, 32]. This method gives the dislocation density and the twin-boundary frequency with good statistics, where the twin-boundary frequency is defined as the fraction of twin boundaries among the $\{111\}$ lattice planes.

The microstructure of the ECAP- and HPT-processed samples was examined by TEM using a Philips CM-20 microscope operating at 200 kV. The TEM samples were mechanically thinned to $\sim 50 \mu\text{m}$, cooled to liquid nitrogen temperature and then thinned with 6 keV Ar^+ ions from both sides until perforation. Finally, a thin damaged layer was removed using 2 keV Ar^+ ions. The axial inhomogeneity of the grain structure in the HPT-processed specimen was studied on the cross-section of the disk by electron backscatter diffraction (EBSD) using a FEI Quanta 3D scanning electron microscope. First, the investigated surface was mechanically polished using an alumina suspension with an average particle size of 50 nm. Then a rectangular area of the surface with dimensions of $100 \times 100 \mu\text{m}^2$ was fine-milled by focused ion beam (FIB) of Ga^+ ions with an inclination angle of 3° to the surface using an accelerating voltage of 30 kV and an ion current of 15 nA. The finest step size in the EBSD experiments was 80 nm.

To examine the axial inhomogeneity of the HPT-sample, nanohardness measurements were carried out on the cross-sections at the center, half-radius and periphery of the disk using a UMIS nanoindentation device with a Berkovich indenter and applying a maximum load of 5 mN. In each location, a series of 400 indentations was recorded with the indents arranged in a 10×40 matrix with a

distance of 15 μm between neighboring indents (see Fig. 2). The indentation measurement was started and finished at a distance of 25 μm from the top and bottom surfaces of the disk and forty indentations were made parallel to the axial direction which corresponds to the total thickness of the disk (650 μm). This process was repeated ten times, giving ten hardness values at each position along the axial direction. These values were then averaged and plotted as a function of the distance from the mid-plane of the disk.

The thermal stability of the ECAP- and HPT-processed specimens was investigated by DSC using a Perkin Elmer (DSC2) calorimeter at a heating rate of 10 K/min. The heat released during annealing was determined as the area under the exothermic peak detected in the thermograms.

Experimental results

Microstructure after processing by ECAP and HPT

The mean grain sizes in the initial material and after one pass of ECAP were ~ 56 and ~ 20 μm , respectively, as shown in the SEM images of Fig. 3a, b. The TEM investigations revealed that after 4 passes of ECAP the mean grain size decreased to about 200 nm, and further ECAP deformation caused only a slight change in the grain size. As an example Fig. 3c shows a bright field TEM image on the sample processed by 8 ECAP passes.

The dislocation density and the twin-boundary frequency values determined by X-ray line profile analysis are listed in Table 1. It is noted that both the dislocation density and the twin-boundary frequency values are exceptionally high compared to other pure fcc metals processed by ECAP [33]. This is due to the limited annihilation of the highly dissociated dislocations and the easy twinning in Ag due to the low SFE (16–22 mJ/m^2 [34, 35]). It can be seen that the dislocation

density increased up to 8 passes of ECAP, reaching a very high ($\sim 46 \pm 5 \times 10^{14} \text{ m}^{-2}$) saturation value, then further ECAP passes up to 16 caused a decrease in the dislocation density to $\sim 33 \pm 4 \times 10^{14} \text{ m}^{-2}$. Similarly, the twin-boundary frequency reached its maximum of $\sim 0.8 \pm 0.1$ % after 4 passes, then it decreased as the deformation proceeded up to 16 passes. A detailed explanation of these tendencies has already been given in an earlier study [36]. In brief, the twin sources are usually located at dislocation glide obstacles such as Lomer–Cottrell locks or grain boundaries where the local stress exceeds the critical stress needed for twin nucleation [37]. The larger dislocation density with increasing number of passes increased the number of twin nucleation sites at glide obstacles, thereby leading to a higher twin-boundary frequency. After 4 passes the grain size was reduced to ~ 200 nm and, due to the large number of grain boundaries, the twins are mainly nucleated at the grain boundaries as was already observed for other nanomaterials [38]. The impurities in solid solution are usually segregated at grain boundaries during SPD at RT [39] which hinders the dissociation of dislocations into twinning partials at grain boundaries. In addition, the interaction of dislocations and twins give untwinning inside the grains [37], so that the reduced activity of twin sources at the grain boundaries leads to a significant decrease in the total twin-boundary frequency after 16 passes. The decrease of the dislocation density between 8 and 16 passes might be caused by a structural recovery in the grain boundaries including the annihilation of extrinsic (or non-geometrically necessary) dislocations, and also the interaction between twin boundaries and dislocations in the untwinning process. A similar decrease of the dislocation density due to dynamic recovery was observed also in Cu processed by more than 8 passes in ECAP [40].

Figure 4 shows the nanohardness distribution measured at the center, half-radius and periphery of the cross-section of the HPT-processed sample as a function of the distance from the mid-plane of the disk. Each value was an average hardness obtained from ten indentations placed at the same distance from the mid-plane. The hardness values reveal significant inhomogeneity in the microstructure along the axial direction. An approximately 150 μm wide surface region with a high hardness of 1.9 ± 0.1 GPa was found at both the bottom and the top of the disk. As the hardness measurements were started and finished about 25 μm beneath the top and bottom surfaces, the thickness of these surface layers is most probably ~ 175 μm . In the internal region near the mid-plane with a thickness of ~ 300 μm the nanohardness was about 1.0 ± 0.1 GPa which is very close to the value determined for the initial annealed sample (see Fig. 3 in [41]). It should be noted that the value of hardness strongly depends on the load applied during its measurement. The hardness usually increases with decreasing the load (or the contact surface area) which is explained by the imperfect geometry of the head [42], the friction between the tip and the

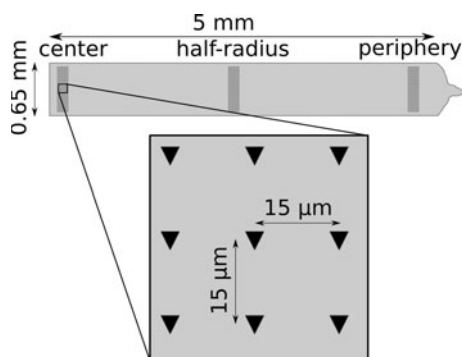


Fig. 2 Nanoindentation layout on the cross-section of the HPT-processed disk

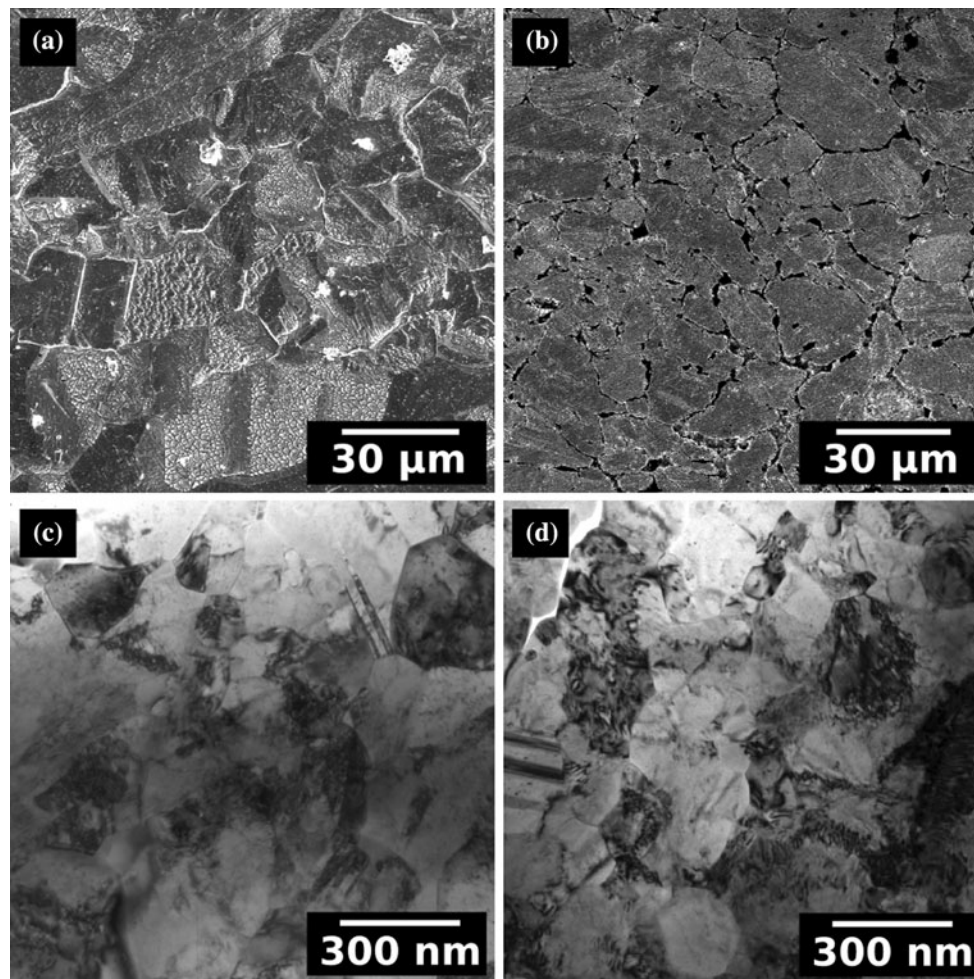


Fig. 3 SEM images illustrating the grain structures in the initial annealed sample (a) and after one pass of ECAP (b). Bright field TEM images showing the microstructures in the sample processed by

8 passes of ECAP (c) and in the surface region of the HPT-sample after one revolution (d)

Table 1 The average grain size (d) determined by TEM, the dislocation density (ρ) and the twin-boundary frequency (β) obtained by XLPA

SPD processing	d (nm)	ρ (10^{14} m^{-2})	β (%)	E_{HAGB} (J/g)	E_{disl} (J/g)	E_{twin} (J/g)	E_{sum} (J/g)	E_{DSC} (J/g)
1 ECAP	20000 ± 3000	26 ± 4	0.4 ± 0.1	<0.01	0.19 ± 0.05	0.01	0.20 ± 0.05	0.30 ± 0.05
4 ECAP	200 ± 30	41 ± 5	0.8 ± 0.1	0.36 ± 0.04	0.28 ± 0.06	0.02	0.66 ± 0.10	0.59 ± 0.04
8 ECAP	200 ± 20	46 ± 5	0.6 ± 0.1	0.36 ± 0.04	0.32 ± 0.06	0.02	0.70 ± 0.10	0.62 ± 0.04
16 ECAP	200 ± 20	33 ± 4	0.3 ± 0.1	0.50 ± 0.05	0.24 ± 0.06	0.01	0.75 ± 0.11	0.72 ± 0.04
1 HPT	230 ± 30	90 ± 9	0.8 ± 0.1	0.16 ± 0.02	0.38 ± 0.10	0.01	0.55 ± 0.12	0.41 ± 0.04

The stored energies for various lattice defects as calculated using Eqs. (1–4). E_{HAGB} high-angle grain boundaries, E_{disl} dislocations, E_{twin} twin boundaries, E_{sum} is the sum of the three calculated stored energies, while E_{DSC} is the released heat determined experimentally by DSC. The values of the quantities and the errors are rounded to two decimal places

material [43], or the strain gradient plasticity [44]. This phenomenon is referred to as indentation size effect (ISE) [42–44]. According to earlier experiments [41], the ratio of the nano- and microhardness values measured at forces of 5 mN and 2 N, respectively, on pure annealed or ECAP-processed Ag is about 2.1 ± 0.4 .

According to the hardness measurements there are very sharp transition layers with thicknesses of less than $30 \mu\text{m}$ between the harder surface regions and the softer internal region. These transition layers are indicated by dashed lines in the SEM image of Fig. 5a. Significant differences were not observed between the hardness distributions measured at the

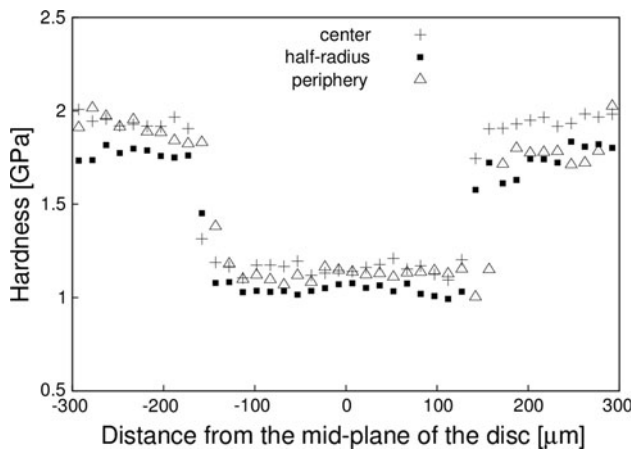


Fig. 4 Nanohardness distribution as a function of the distance from the mid-plane in the axial direction measured on the cross-section of the disk processed by one revolution of HPT

center, half-radius and periphery. In addition, the hardness values obtained for the top and bottom surface layers agree within the experimental error. In order to reveal the reason for the hardness inhomogeneity, the transition region between the soft and hard volumes was investigated also by EBSD. Figure 5b shows the grain structure in the vicinity of the upper transition layer at the half-radius of the disk. The layer is very sharp with a roughness of about 5 μm in accordance with the hardness measurements. Above the transition layer the high hardness is caused by the UFG microstructure. Below this layer, a recrystallized microstructure was observed which may explain the much lower hardness value in the interior of the sample. The mean size of the grains in the recrystallized volume was about 50 μm , similar to the initial annealed material.

The microstructure in the hard surface layer of the HPT-processed disk was investigated by TEM and XLP. In the case of TEM, the sample was mainly thinned from one side of the disk, therefore finally the specimen was perforated at 50 μm beneath the surface layer on the other side of the sample. The TEM image in Fig. 3d illustrates that the mean grain size at the half-radius near the surface of the disk was 230 ± 30 nm (as obtained from several images). The dislocation density and the twin-boundary frequency were determined on the surface of the HPT-processed disk. Since the penetration depth of X-rays in Ag is less than the surface layer thickness of ~ 175 μm , therefore the defect densities obtained by XLP characterize only this hard layer. The dislocation density and the twin-boundary frequency were $\sim 90 \pm 9 \times 10^{14} \text{ m}^{-2}$ and $\sim 0.8 \pm 0.1$ %, respectively, after one revolution in HPT. Neither the grain size nor the defect densities exhibited significant change along the radius of the disk. The dislocation density in the HPT-processed sample was much higher than the values measured for the ECAP samples. The higher value of the

dislocation density can be explained by the very high applied pressure (6 GPa) during the HPT process, which retards vacancy diffusion, thereby hindering the climb-controlled dislocation annihilation as was discussed in earlier research [9].

Thermal stability of the UFG microstructure in ECAP- and HPT-processed samples

During the DSC-scan up to 800 K a single exothermic peak was obtained for each sample which corresponds to recovery and recrystallization of the UFG microstructure as shown by earlier XLP investigations [19]. These exothermic peaks are plotted in Fig. 6 for the ECAP- and HPT-processed samples. The areas under the peaks represent the experimental heat values (E_{DSC}) released during recovery and recrystallization which are listed in Table 1. The sample processed by one pass of ECAP has the highest peak temperature (see the insert in Fig. 6) due to the lowest densities of lattice defects and the largest grain size which yield a small driving force for recovery and recrystallization. With increasing numbers of passes, the peak maximum was shifted to lower temperature together with an increase of the released heat. For the sample processed by one revolution of HPT, the released heat is relatively small despite the very high defect density determined by XLP. This can be explained by the lack of considerable stored energy in the internal recrystallized volume.

Discussion

The present experimental results reveal a significant difference between the thermal stability of the UFG silver samples processed in different ways by SPD. With increasing numbers of passes in ECAP, the temperature of the DSC peak maximum and the released heat decreases and increases, respectively. Most probably, these changes are not independent of each other as the larger stored energy yields a higher driving force for recovery and recrystallization, resulting in an earlier heat release during annealing in DSC. However, in the case of the HPT-processed specimen, the relatively low released heat is accompanied by a low temperature of recovery and recrystallization. For this sample, the heat released is low and similar to the value obtained for the specimen processed by 1 pass of ECAP (see Table 1), while the DSC peak maximum appears at a relatively low temperature which is similar to 4–16 ECAP samples having a high released heat. In addition, the much larger dislocation density in the HPT specimen compared to the 4–16 ECAP samples predicts a higher stored energy although the released heat for the former specimen is lower. This

Fig. 5 a SEM image showing the peripheric side of the cross-section of the HPT-processed disk. The dashed lines represent the transition layers between the hard surface layers and the soft internal region as determined by nanoindentation (see Fig. 4). The sample was embedded in a non-conducting dentacryl polyamid, therefore very bright patches appear outside of the sample on the right side of the micrograph. **b** EBSD micrograph showing the UFG surface region and the recrystallized volume in the vicinity of the upper transition layer at the half-radius of the disk

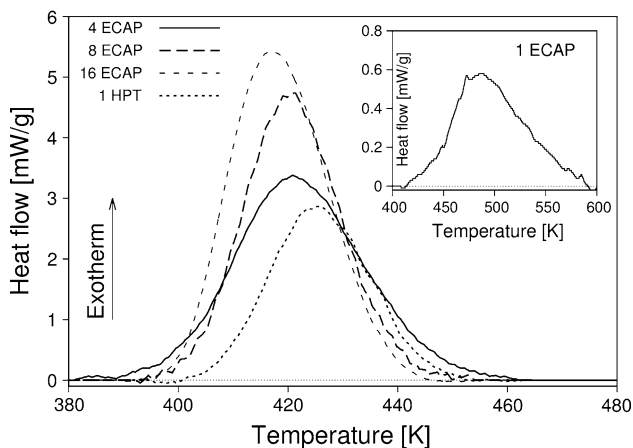
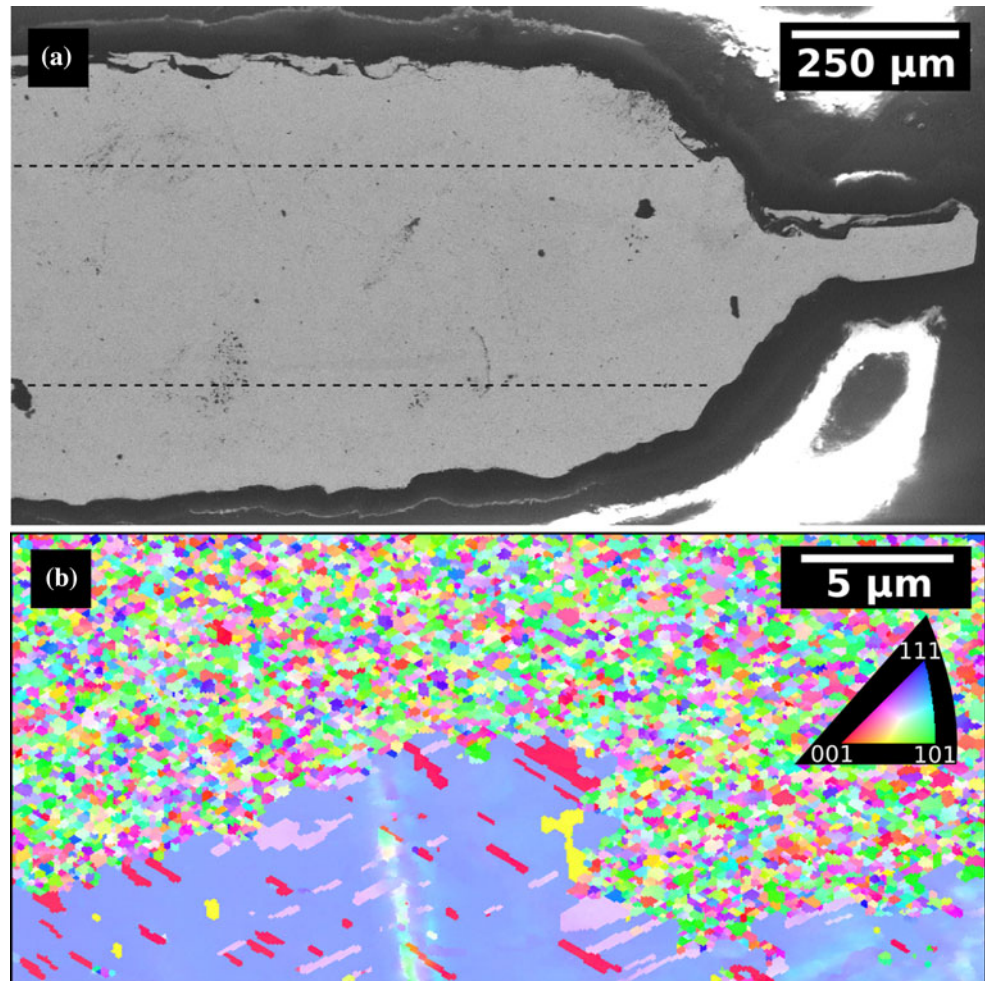


Fig. 6 DSC thermograms obtained at a heating rate of 10 K/min for the samples processed by 1, 4, 8, and 16 passes of ECAP and one revolution of HPT

dichotomy can be explained by the heterogeneous microstructure of the HPT-processed disk along its axial direction. The volume in the middle of the disk with a thickness of $\sim 300 \mu\text{m}$ contains recrystallized grains as shown in

Fig. 5b, therefore this part makes no contribution to the released heat, resulting in a relatively low value for the area under the DSC peak. The outer surface layers of the disk exhibit very fine grains with extremely high dislocation density which lead to an earlier recovery and recrystallization during heating in the DSC experiments.

Large heterogeneity in microstructure and hardness along the axial direction of HPT-processed disks has already been observed for other materials, such as pure Cu [45], Al–Mg–Sc solid solution [46], Mg-alloys [47–49], and the Zr_3Al intermetallic compound [50]. For instance, in an AZ31 Mg-alloy processed by HPT up to one revolution at RT or 463 K the hardness was the highest in the vicinity of the mid-plane due to the very fine grain structure [47–49]. The surface layers with a thickness of about $150 \mu\text{m}$ exhibited a large grained microstructure, yielding a smaller hardness. Similar heterogeneity of the grain structure along the axial direction has been observed for Cu [45]. The finer grain structure around the mid-plane was caused by a larger plastic strain in the middle of the specimens as revealed by the shear patterns observed on the cross-sections of HPT-processed disks [47]. The larger

strains in the middle of the disks are most probably caused by the outflow of the material between the anvils of the HPT facility (see Fig. 1) [45]. Similar to silver in this study, very thin transition layers between the UFG and coarse-grained regions were observed for AZ31 Mg-alloy [48] and Zr₃Al intermetallic compound [50]. The explanation of the sharpness of this layer needs further investigations.

The inhomogeneity of the microstructure and the hardness distribution in the cross-section are influenced by the disk thickness and the friction coefficient between the sample and the anvil surfaces [46, 51]. The finer grain structure and the higher hardness in the middle of HPT-processed disks were observed in Cu, Al-, and Mg-alloys, while in 99.99 % purity Al the microstructure exhibits excellent homogeneity throughout the disk [52]. In the latter case, the high SFE and the low melting point yielded an easy recovery by cross-slip or climb of dislocations, therefore a dynamic equilibrium between the formation and annihilation of dislocations was readily achieved in the whole specimen during HPT. However, in Cu having a medium SFE or in solid solutions, the annihilation of dislocations is retarded and therefore the strain differences lead to large deviations in the microstructure and the hardness. In the case of Ag, the low SFE makes recovery difficult and therefore a very large dislocation density was achieved in the surface region. However, in the middle of the disk, where the strain is larger, the UFG microstructure may be recrystallized since low SFE facilitates recrystallization in heavily deformed pure metals, as noted earlier [27]. This effect yielded lower hardness in the middle of the HPT-processed disk, which is a unique behavior compared to any other observations in the literature, as the internal volumes are usually harder than the surface layers.

The correlation between the parameters of the microstructure and the heat released during DSC experiments was investigated by calculating the energies stored in the ECAP- and HPT-processed specimens. The stored energy per unit mass in the UFG Ag samples is determined as the sum of the energies of the lattice defects (grain boundaries, dislocations, and twin faults). It is noted that the values of the calculated energies in this report are rounded to the precision of the measured released heat in DSC which corresponds to two decimal places. The energy stored in dislocations (E_{disl}) can be determined from the dislocation density using the following relationship [33]:

$$E_{\text{disl}} = A \frac{Gb^2\rho}{\rho_m} \ln \frac{1}{b\sqrt{\rho}}, \tag{1}$$

where G is the shear modulus (30 GPa), b is the magnitude of Burgers vector (0.29 nm), ρ is the dislocation density, ρ_m is the mass density ($10.5 \times 10^6 \text{ gm}^{-3}$), and A denotes a

factor which depends on the edge/screw character of the dislocations. The value of A is equal to $(4\pi)^{-1}$ and $(4\pi\nu(1 - \nu))^{-1}$ for screw and edge dislocations, respectively, where ν is Poisson's ratio (taken as 0.3).

The parameter q determined from X-ray line profile analysis describes the edge/screw character of the dislocations. The theoretically calculated values of q for pure edge and screw dislocations in Ag are 1.62 and 2.35, respectively. In practice, the value of A was obtained from the experimentally determined q of 2.2 ± 0.1 using a simple rule of mixtures [9]:

$$A = \frac{q - 1.62}{0.73} \frac{1}{4\pi} + \frac{2.35 - q}{0.73} \frac{1}{4\pi(1 - \nu)}. \tag{2}$$

In our previous work [19], it was found for Ag processed by 4 ECAP passes that the dislocation density immediately before the DSC peak was about 20 % smaller than in the as-processed state due to partial recovery. Therefore, in order to compare the calculated and the experimentally determined values of the released heat, the dislocation density was reduced by 20 % before its substitution into Eq. (1). The stored energies calculated for dislocations in the ECAP- and HPT-processed samples are listed in Table 1. In the case of the HPT specimen, the energy obtained from Eq. (1) was reduced by half, because the measured dislocation density was valid only for the two UFG surface layers which occupy only about one-half of the total volume. In the internal recrystallized region the dislocation density is lower than the detection limit of XLP, $\sim 10^{13} \text{ m}^{-2}$, which is about three orders of magnitude smaller than the dislocation density in the surface layer, therefore its contribution to the total stored energy is negligible.

The interfaces between the grains can be classified as low- and high-angle grain boundaries (LAGBs and HAGBs, respectively). The LAGBs usually consist of dislocations and XLP measures dislocations in both the boundaries and the interiors of the grains so that the contribution of LAGBs to the stored energy is incorporated in Eq. (1). The energy of the HAGBs (E_{HAGB}) is given as [53]:

$$E_{\text{HAGB}} = h \frac{3\gamma_{\text{GB}}}{d\rho_m}, \tag{3}$$

where γ_{GB} is the average HAGB energy in Ag (0.5 J/m² [54]), h is the fraction of HAGBs, and d is the average grain size. The value of h was selected as 0.1 for 1 pass, 0.5 for 4 and 8 passes, and 0.7 for 16 passes of ECAP according to the HAGB fractions obtained on other pure fcc metals for similar ECAP passes (e.g., for Al [55]). In the case of HPT-processed sample, the average fraction of HAGBs was estimated by the value of 0.5 obtained for Cu deformed by one revolution of HPT [56]. For Ag processed

by HPT, the value of E_{HAGB} calculated by Eq. (3) was also reduced by half, since the internal recrystallized volume with more than two orders of magnitude larger grain size makes a negligible contribution to the stored energy.

The stored energy for twin faults (E_{twin}) in cubic grains can be calculated as [19]

$$E_{\text{twin}} = \gamma_{\text{twin}} d^2 \frac{d}{d_{\text{twin}} d^3 \rho_m} = \frac{\gamma_{\text{twin}} \beta}{d_{111} \rho_m}, \quad (4)$$

where γ_{twin} is the twin-boundary energy in Ag, β is the twin-boundary frequency determined by XLP, d_{111} is the spacing between the neighboring {111} planes (0.24 nm) and d_{twin} is the mean twin-boundary spacing which can be expressed as d_{111}/β . For the HPT-processed specimen, the stored energy calculated by Eq. (4) was also reduced by half, as the twin-boundary frequency was negligible in the recrystallized volume. The values of E_{twin} for all the investigated samples were 0.01–0.02 J/g as shown in Table 1, therefore twin boundaries make only a marginal contribution to the stored energy.

Table 1 also shows the sum of the calculated contributions of the dislocations, HAGBs and twin boundaries to the released heat which agrees well with the measured values within the experimental error for all the studied samples. It should be noted that, in addition to dislocations and boundaries, other lattice defects such as vacancies or vacancy agglomerates might also make contributions to the released heat, however these effects are negligible. For instance, the stored energy corresponding to a high vacancy concentration of 10^{-5} is only ~ 0.01 J/g which is marginal compared to the contributions of dislocations and HAGBs.

Conclusions

1. The dislocation density in the ECAP- and HPT-processed specimens was very high due to the high degree of dislocation dissociation due to the low SFE which hindered the annihilation of dislocations during SPD. In the HPT-sample, the dislocation density was much higher than in the ECAP-processed samples as the high pressure in HPT retarded vacancy diffusion and thereby impeded the annihilation of dislocations by climb.
2. For ECAP-processed Ag, the maximum of the exothermic DSC peak was shifted to a lower temperature while the released heat increased with increasing numbers of passes. The sum of the energies stored in HAGBs and dislocations agreed well with the experimental value of the released heat obtained by DSC.
3. The sample processed by one revolution of HPT exhibited a very heterogeneous microstructure in the axial direction of the disk. A hard UFG microstructure

on the surfaces and a soft recrystallized internal region in the middle of the disk with similar volume fractions were observed. As a consequence, the released heat determined by DSC was relatively small despite the very high dislocation density in the surface layers.

Acknowledgements This study was supported in part by the Hungarian Scientific Research Fund, OTKA, Grant No. K-81360, in part by the National Science Foundation of the United States under Grant No. DMR-1160966 (MK and TGL) and in part by the European Research Council under ERC Grant Agreement No. 267464-SPD-METALS (TGL). The authors thank Ms. Noémi Szász for preparation of the TEM samples as well as Dr. Zoltán Dankházi, Dr. Károly Havancsák and Mr. Gábor Varga for performing SEM/EBSD experiments. The help of Mr. Péter Szommer in nanohardness experiments is also acknowledged.

References

1. Segal VM (1999) *Mater Sci Eng A* 271:322
2. Valiev RZ, Islamgaliev RK, Alexandrov IV (2000) *Prog Mater Sci* 45:103
3. Valiev RZ, Langdon TG (2006) *Prog Mater Sci* 51:881
4. Zhilyaev AP, Langdon TG (2008) *Prog Mater Sci* 53:893
5. Cao WQ, Godfrey A, Liu W, Liu Q (2003) *Mater Sci Eng A* 360:420
6. Molodova X, Gottstein G, Winning M, Hellmig RJ (2007) *Mater Sci Eng A* 460–461:204
7. Cao WQ, Gu CF, Pereloma EV, Davies CHJ (2008) *Mater Sci Eng A* 492:74
8. Zhilyaev AP, Nurislamova GV, Surinach S, Baró MD, Langdon TG (2002) *Mater Phys Mech* 5:23
9. Gubicza J, Dobatkin SV, Khosravi E, Kuznetsov AA, Lábár LJ (2011) *Mater Sci Eng A* 528:1828
10. Gubicza J, Nam NH, Balogh L, Hellmig RJ, Stolyarov VV, Estrin Y, Ungár T (2004) *J Alloys Compd* 378:248
11. Gubicza J, Balogh L, Hellmig RJ, Estrin Y, Ungár T (2005) *Mater Sci Eng A* 400–401:334
12. Huang YK, Menovsky AA, de Boer FR (1993) *Nanostruct Mater* 2:587
13. Kumpmann A, Günther B, Kunze H-D (1993) *Mater Sci Eng A* 168:165
14. Zhilyaev AP, Nurislamova GV, Valiev RZ, Baró MD, Langdon TG (2002) *Metall Mater Trans A* 33:1865
15. Cizek J, Prochazka I, Cieslar M, Kuzel R, Kuriplach J, Chmelik F, Stulikova I, Becvar F, Melikhova O (2002) *Phys Rev B* 65:094106
16. Zhilyaev AP, Gubicza J, Nurislamova G, Révész Á, Surinach S, Baró MD, Ungár T (2003) *Phys Stat Sol A* 198:263
17. Zhilyaev AP, Kim B-K, Szpunar JA, Baró MD, Langdon TG (2005) *Mater Sci Eng A* 391:377
18. Lugo N, Llorca N, Sunol JJ, Cabrera JM (2010) *J Mater Sci* 45:2264
19. Hegedűs Z, Gubicza J, Kawasaki M, Chinh NQ, Süvegh K, Fogarassy Z, Langdon TG (2013) *J Mater Sci* 48:1675
20. Tjong SC, Chen H (2004) *Mater Sci Eng R* 45:1
21. Kuo C-M, Lin C-S (2007) *Scr Mater* 57:667
22. Setman D, Schafner E, Korznikova E, Zehetbauer MJ (2008) *Mater Sci Eng A* 493:116
23. Setman D, Kerber MB, Schafner E, Zehetbauer MJ (2010) *Metall Mater Trans A* 41:810

24. Wang G, Wu SD, Zuo L, Esling C, Wang ZG, Li GY (2003) *Mater Sci Eng A* 346:83
25. Estrin Y, Isaev NV, Lubenets SV, Malykhin SV, Pugachov AT, Pustovalov VV, Reshetnyak EN, Fomenko VS, Fomenko LS, Shumilin SE, Janecek M, Hellmig RJ (2006) *Acta Mater* 54:5581
26. Matsunaga M, Horita Z (2009) *Mater Trans* 50:1633
27. Gubicza J, Chinh NQ, Lábár LJ, Hegedús Z, Langdon TG (2010) *Mater Sci Eng A* 527:752
28. Hegedús Z, Gubicza J, Kawasaki M, Chinh NQ, Fogarassy Z, Langdon TG (2011) *Mater Sci Eng A* 528:8694
29. Furukawa M, Iwahashi Y, Horita Z, Nemoto M, Langdon TG (1998) *Mater Sci Eng A* 257:328
30. Iwahashi Y, Wang J, Horita Z, Nemoto M, Langdon TG (1996) *Scr Mater* 35:143
31. Ribárik G, Gubicza J, Ungár T (2004) *Mater Sci Eng A* 387–389:343
32. Balogh L, Ribárik G, Ungár T (2006) *J Appl Phys* 100:023512
33. Schafner E, Steiner G, Korznikova E, Kerber M, Zehetbauer MJ (2005) *Mater Sci Eng A* 410–411:169
34. Hirth JP, Lothe J (1982) *Theory of dislocations*. Wiley, New York
35. Murr LE (1975) *Interfacial phenomena in metals and alloys*. Addison Wesley, Reading
36. Gubicza J, Chinh NQ, Lábár LJ, Hegedús Z, Langdon TG (2009) *J Mater Sci* 44:1656
37. Müllner P, Solenthaler C (1997) *Mater Sci Eng A* 230:107
38. Zhu YT, Wu XL, Liao XZ, Narayan J, Mathaudhu SN, Kecskés LJ (2009) *Appl Phys Lett* 95:031909
39. Liddicoat PV, Liao X-Z, Zhao Y, Zhu Y, Murashkin MY, Lavernia EJ, Valiev RZ, Ringer SP (2010) *Nat Commun* 1:63
40. Dalla Torre F, Lapovok R, Sandlin J, Thomson PF, Davies CHJ, Pereloma EV (2004) *Acta Mater* 52:4819
41. Gubicza J, Chinh NQ, Lábár LJ, Hegedús Z, Szommer P, Tichy G, Langdon TG (2008) *J Mater Sci* 43:5672
42. Mencik J, Swain MV (1995) *J Mater Res* 10:1491
43. Li H, Bradt RC (1993) *J Mater Sci* 28:917
44. Nix WD, Gao H (1998) *J Mech Phys Solids* 46:411
45. Jeong HJ, Yoon EY, Lee DJ, Kim NJ, Lee S, Kim HS (2012) *J Mater Sci* 47:7828
46. Sakai G, Nakamura K, Horita Z, Langdon TG (2005) *Mater Sci Eng A* 406:268
47. Figueiredo RB, Aguilar MTP, Cetlin PR, Langdon TG (2011) *Metall Mater Trans A* 42A:3013
48. Figueiredo RB, Langdon TG (2011) *Mater Sci Eng A* 528:4500
49. Kawasaki M, Figueiredo RB, Langdon TG (2012) *J Mater Sci* 47:7719
50. Geist D, Rentenberger C, Karnthaler HP (2011) *Acta Mater* 59:4578
51. Figueiredo RB, Aguilar MTP, Cetlin PR, Langdon TG (2012) *J Mater Sci* 47:7807
52. Kawasaki M, Figueiredo RB, Langdon TG (2011) *Acta Mater* 59:308
53. Humphreys FJ, Hatherly M (2004) *Recrystallization and related annealing phenomena*, 2nd edn. Elsevier, Oxford
54. Wolf D (1984) *Acta Metall* 32:735
55. Kawasaki M, Horita Z, Langdon TG (2009) *Mater Sci Eng A* 524:143
56. An XH, Wu SD, Zhang ZF, Figueiredo RB, Gao N, Langdon TG (2010) *Scr Mater* 63:560